Carbon nanotubes with rich pyridinic nitrogen for gas phase CO_2 electroreduction

Chen Ma[a,d], Pengfei Hou[a,d], Xiuping Wang[c], Zhuo Wang[a], Wenting Li[a,d], Peng Kang[a,b,c,*]

[a] Key Laboratory of Photochemical Conversion and Optoelectronic Materials, Technical Institute of Physics and Chemistry, Chinese Academy of Sciences, Beijing, 100190, PR China
[b] School of Chemical Engineering and Technology, Tianjin University, 135 Yaguan Rd, Tianjin, PR China
[c] Carbon Energy Technology Co. Ltd., Yancun Industrial Park, Funhill, Beijing, PR China
[d] University of Chinese Academy of Sciences, Chinese Academy of Sciences, Beijing, 100190, PR China

ARTICLE INFO

ABSTRACT

Nitrogen doped carbon nanotubes (NCNTs) with high concentration of pyridinic N sites (62.3% of all nitrogen) were prepared by pyrolysis of phenathroline heterocycle precursor, and they can reduce CO_2 to CO with high selectivity and stability. Faradaic efficiency of CO maintained > 94.5% between -0.6 to -0.9 V vs the reversible hydrogen electrode (RHE), and the CO current density was as high as 20.2 mA cm^{-2}. Moreover, during 40 h electrolysis at -0.8 V, Faradic efficiency for CO was stable at 95%. The high performance came from rich concentrations of pyridine N sites in NCNTs, serving as the active sites for catalysis. Furthermore, gas phase CO_2 electrolysis showed nearly 100% Faradic efficiency for CO, suggesting that the NCNT can maximize the CO_2 reduction efficiency and hydrogen evolution was suppressed completely.

1. Introduction

As climate change becomes more prominent [1], many solutions have been developed for reduction of CO_2, such as electrochemical, photochemical and biological methods [2,3]. Despite many challenges, electrochemical reduction is promising for conversion of CO_2 to fuels and chemicals with renewable energy [4–10]. However, CO_2 is very stable, and electrocatalytic reduction often suffers from high over-potential, slow kinetics, low product selectivity and catalyst stability [11–13]. Noble metal electrodes exhibit high selectivity and stability for reduction of CO_2 at relatively low over-potential [14–18]. In addition, catalysts based on inexpensive materials are recently being explored such as Sn [19–21], Cu [22,23], Co [24–27] and carbon materials [28–30], etc.

Nitrogen-doped carbon materials are efficient catalysts for CO_2 electroreduction [9,13,31]. Nitrogen-doped carbon nanofiber exhibited small overpotential for CO_2 reduction in ionic liquids [28]. N-doped graphene quantum dot produced multi-carbon products such as ethanol, acetate and n-propanol, although the product selectivity of each was relatively low [29]. Recently, nitrogen-doped mesoporous carbon was used to reduce CO_2 to ethanol with high efficiency and selectivity (77%) in aqueous media [30]. Other N-doped materials, such as N-doped graphene [32–34], diamond and carbon [35,36] have also

been reported for CO_2 reduction reaction (Table S1).

Among N-doped carbons, N-doped carbon nanotubes gained much attention for CO_2 reduction and other electrocatalysis [37], because of unique electronic and geometric features [38]. Polyethylenimine-modified NCNTs can reduce CO_2 to formate with high selectivity (87%) and current density in aqueous media [39]. Chemical vapor deposition (CVD) prepared NCNT arrays showed high selectivity of 80% for CO at a low overpotential of 0.26 V [40]. The superior activity for this NCNT array was attributed to high density of pyridinic N sites (27% of all Ns) [41]. NCNTs catalysts synthesized by the calcination of polymers can achieve a maximum current efficiency of 90% for CO formation at a potential of -0.9 V vs RHE with pyridinic N content of 32% [42]. However, those NCNTs catalysts also suffer from low CO current density compared with noble-metal catalysts. Increasing the N concentration is critical for more efficient catalysts.

Among those nitrogen-doped carbon materials, pyridinic N is regarded as the most important catalytic site for carbon dioxide reduction reaction (CO_2RR). Graphitic N defects are less capable for CO_2 binding, and pyrrolic N defects have little or no impact on the CO_2RR activity. However, the atomic abundance of the pyridinic N in most catalysts was low, mostly ca 30% of all N atoms, and only a few materials can reach ca 60% pyridinic N (Table S1). Therefore, increasing the density of pyridinic N defects is critical. Pyrolysis is an effective method to

prepare NCNTs with high N content [33–35]. Herein, phenathroline was used as precursor to increase the pyridine N concentration. The influence of N doping and atomic configurations on activity was investigated and catalytic active sites were identified. In addition, the mechanism of CO_2RR on NCNTs was proposed.

To further maximize the CO_2 reduction efficiency, gas phase CO_2 electrolysis was performed. As water can compete with the adsorption of CO_2 on N sites in aqueous phase [34,36], gas phase CO_2 electrolysis is a promising approach to maximize the CO_2 reduction efficiency with accelerated mass transfer and increased surface adsorption of CO_2 [43–46]. Pyridinic N sites with high basicity could concentrate CO_2 on surface which is favorable to subsequent CO_2RR [39]. Reaction of CO_2 at solid − gas interface not only overcomes the low solubility limitations in aqueous phase, but also increases CO_2 adsorption at the active sites [47]. The pyridinic N rich NCNT with surface CO_2 enrichment can be synergetic with gas phase electrolysis to increase the catalytic activity.

2. Experimental

2.1. Materials and catalyst preparation

$NaHCO_3$ (99.5%), ethanol (99.7%) and nitric acid were purchased from Beijing Chemical Works. 1,10-Phenanthroline monohydrate was purchased from Jiuding Chemistry. Multi-walled carbon nanotube was purchased from XFNano Company. Ar (99.999%), and CO_2 (99.999%) were purchased from the Beijing Qianxi Gas Company. NH_3 (99.999%) was purchased from Beijing Chengxinshunxing Gas Company. Nafion® 117 membrane was purchased from DuPont. Electrolyte solutions were prepared with DI water.

In the preparation of NCNT-NH_3, 600 mg of 1,10-phenanthroline monohydrate was dissolved in a mixture of 25 ml of ethanol and 25 ml of deionized water. Then, 200 mg of multi-walled carbon nanotube (MWCNT) (nitric acid was applied first to remove metal ions) was added and stirred for 12 h at room temperature. The dispersions was heated to evaporate the solvent and dried in an oven at 105 °C for 12 h. Then, grinding the mixture into a powder in an agate mortar yielded precursor of NCNT. Finally, the NCNT-NH_3-700 (or NCNT-NH_3 for short) and NCNT-Ar were prepared by the calcination of precursor under NH_3 and Ar atmosphere (100 sccm) at 700 °C for 3 h, respectively. The temperature in the calcination was controlled by the temperature-programmed reaction (TPR) with a heating rate of 5 °C min^{-1} and a cooling rate of 3.3 °C min^{-1}. The precursor of NCNT was also calcined at 300 °C and 500 °C for 3 h under NH_3 to obtain NCNT-NH_3-300 and NCNT-NH_3-500, respectively. The CNT-NH_3 and CNT-Ar were prepared by calcination of the original MWCNT at 700 °C for 3 h under NH_3 and Ar atmosphere, respectively. The catalysts were listed in Table 1.

2.2. Catalyst characterization

The morphology of NCNTs catalysts were characterized by JEOL JEM-2100 F transmission electron microscopy (TEM) and field-emission scanning electron microscopy (FESEM; S-4800, Hitachi). X-ray diffraction analyses (XRD) were collected on a Bruker DAVINCI D8 ADVANCE diffractometer using a Cu Kα source (λ = 1.54184 nm). X-ray diffraction spectra were obtained for 2 θ values differing from 10 to 90 degrees with a step length of 0.1 °. Raman spectra were recorded from 200 to 3200 cm^{-1} on an inVia-Reflex confocal laser micro-Raman spectrometer with a CCD detector using Ar$^+$ laser excitation with a wavelength of 532 nm at 10 mW laser power. The microscope was with a 50x telephoto lens. An ESCALAB 250 XI X-ray photoelectron spectroscopy (XPS) of Thermo Scientific was used to analyze the surface electronic structures, using a monochromatic Al Kα radiation (1486.6 eV). A survey scan was performed with a step size of 1 eV, a pass energy of 80 eV, and a dwell time of 200 ms. High resolution scans were then taken for each element present with a step size of 0.1 eV and a pass energy of 20 eV. The binding energy for all peaks was referenced to the C 1 s peak at 284.6 eV. The software of XPSPEAK41 was used for the interpretation/deconvolution of spectra. The peak fitting parameters for XPS were summarized in Table S4 (supporting information). CO_2 adsorption-desorption isotherm was measured on a Quantachrome Autosorb-1-C-TCD instrument.

2.3. Electrochemical measurements

Electrochemical measurements were performed with a CHI660E electrochemistry workstation in an H-cell (separated by Nafion) with a conventional three-electrode system using 0.5 M aqueous electrolyte at room temperature. The Pt wire and saturated calomel reference electrode (SCE) were used as counter electrode and reference electrode, respectively. The measured potentials after iR compensation were rescaled to the RHE by E (vs. RHE) = E (vs. SCE) + 0.245 V + 0.0591 V × pH. The working electrode was prepared as following: 10 mg catalysts and 100 μL of 5 wt % Nafion solution were dispersed in 1 mL ethanol with sonication for 1 h to form a homogeneous ink. 10 μL of the ink was load onto a 3 mm diameter glassy carbon electrode and dried at room temperature before electrochemical tests.

Before the controlled potential electrolysis (CPE), CO_2 (99.999%) was purged into over 30 min to remove the air from electrolyte, then the electrolysis was conducted under sealed conditions. The gaseous products were analyzed by SRI MG-I GC with a helium ionization detector (HID) and had been calibrated using external gas standard. Liquid products were analyzed by solution NMR (Bruker AVNANCE-400) using N, N-dimethylformamide as an internal standard.

The electrochemical surface area (ECSA) of catalysts was calculated from their electrochemical double-layer capacitance (Cdl) and cyclic voltammogram (CV) measurements were performed to obtain Cdl. The potential of CV was ranged from 0.37 to 0.47 V vs RHE with various scan rates (10, 20, 30, 50, 80 and 100 mV s^{-1}) under CO_2 atmosphere. The Cdl was calculated by plotting the Δj = ja − jc at 0.42 V vs the scan rate, in which jc and ja are the cathodic and anodic current densities, respectively. The linear slope was twice that of Cdl. Electrochemical impedance spectroscopy (EIS) measurement was performed in the frequency range of 0.1 to 100,000 Hz with an amplitude of 10 mV at the

Table 1
Brief summary for the preparation of catalysts.

Sample	Catalyst Preparation Condition		
	Precursor	Atmosphere	Temperature (°C)
NCNT-NH_3 (NCNT-NH_3-700)	MWCNT + 1,10-phenanthroline	NH_3	700
NCNT-NH_3-500	MWCNT + 1,10-phenanthroline	NH_3	500
NCNT-NH_3-300	MWCNT + 1,10-phenanthroline	NH_3	300
NCNT-Ar	MWCNT + 1,10-phenanthroline	Ar	700
CNT-NH_3	MWCNT	NH_3	700
CNT-Ar	MWCNT	Ar	700

potential of -0.6 V vs RHE.

The membrane-electrode assembly (MEA) contained anion-exchange membrane (TWEDAI, TianWei Membrane, Inc., China) and anodic and cathodic catalyst layers. Cathode ink was obtained by mixing 25 mg NCNT-NH$_3$-700 with 5 mL n-propyl alcohol and 0.1 mL 5 wt. % anion-exchange resin solution (TWEDAI, TianWei Membrane, Inc., China). The cathode ink was sonicated for 15 min and sprayed onto an anion-exchange membrane of 5 cm^2 active area, and then cold-pressed at 0.6 MPa for 5 min. The anode ink was made of 25 mg iridium black (HeSen, Shanghai, China) with 5 mL n-propyl alcohol and 0.1 mL 5 wt% Nafion solution (DuPont, USA), the mixture was sonicated for 5 min. The anode ink was sprayed onto the above anion-exchange membrane with a 5 cm^2 active area, and then was cold-pressed at 0.6 MPa for 5 min.

Electrochemical flow cell was assembled using 5 cm^2 fuel cell hardware with graphite serpentine flow channels, by sandwiching the MEA with gaskets for sealing and electrical insulation. Titanium mesh was used as the current collector. In the electrolysis, DI water was fed to the anode with the flow rate of 33 sccm by peristaltic pump (BT100 M, EasyPump, Inc., BaoDing, China), and the CO$_2$ stream was humidified at room temperature and fed to the cathode at the flow rate of 30 sccm by using mass flow controller (D07, Sevenstar, Beijing, China). The content of water vapor in CO$_2$ was determined by a hygrometer (DWS-T5, DiHui, Beijing, China). Electrochemical study was performed on CHI 1140C electrochemical station (CHI Instruments, Inc.) in a two electrode electrochemical system with an additional reference electrode for measuring potential only. The gaseous product was analyzed by SRI gas analyzer GC equipped with a Helium Ionization detector (HID, SRI 8610C, USA). The GC used a helium carrier gas and was calibrated using external gas standard.

3. Results and discussion

3.1. Material characterization

Heterocycle 1,10-phenanthroline was used as the main N source to prepare NCNT-NH$_3$ and NCNT-Ar by pyrolysis under ammonia and Ar respectively (Fig. 1a, Table 1). Hypothetical pyrolysis mechanism for 1,10-phenanthroline was proposed in Fig. 1b, which could provide rich and well defined pyridinic nitrogen atoms on surface.

Scanning electron microscopy (SEM) images of NCNT-NH$_3$ showed nanoporous structure (Figs. 2a & S1). The transmission electron microscopy (TEM) image (Fig. 2b) showed structures of the multi-walled carbon nanotube, and the deposited carbon materials could not be resolved. The electron energy loss spectroscopy (EELS) mapping of NCNT-NH$_3$-700 in Fig. 2b revealed that the N and O atoms distributed homogeneously on NCNT-NH$_3$. X-ray diffraction (XRD) (Fig. 2c) showed three diffraction peaks, at 2θ = 27.3°, 43° and 53°, and they were assigned to the (002), (100) and (004) planes, respectively [40]. The Raman spectrum in Fig. 2d showed a D- and G-band at ca.
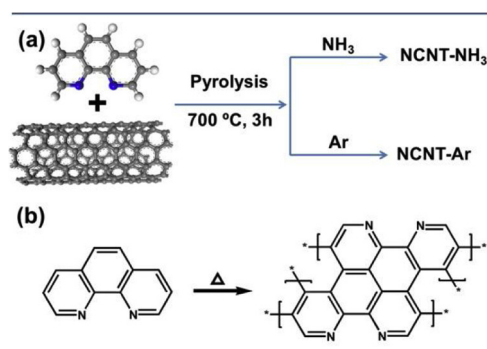

Fig. 1. (a) Schematic illustration of the fabrication of nitrogen doped carbon nanotubes. (b) Proposed pyrolysis mechanism for phenanthroline.

1345 cm^{-1} and 1575 cm^{-1}, respectively. The ratio of D- and G-band (I$_D$/I$_G$) increased from 0.704 to 0.744 after pyrolysis under NH$_3$, which indicates that more defects were created in NCNT-NH$_3$ catalysts.

XPS was used to investigate the amount of N doping and atomic configurations. For the N 1 s spectra of phenanthroline precursor on CNT, pyridinic N atom was fit at ca. 399.0 eV (Fig. S3). The XPS analysis showed that the total N contents of the NCNT-NH$_3$, NCNT-Ar were comparable, at 2.51% and 2.54%, respectively (Figs. 3d & S4). The high-resolution N 1 s spectra of NCNT-NH$_3$ and NCNT-Ar (Fig. 3a & b) were deconvoluted into three sub-peaks at ca. 399.0, 400.4 and 401.2 eV, assigned to pyridinic, pyrrolic and graphitic N, respectively. The pyridinic N and pyrrolic N were the dominant N sites in these materials. The percentage of pyridinic N atoms was 62.3% for NCNT-NH$_3$ and 53.3% for NCNT-Ar of all N atoms. Thus, pyridinic N atoms occupied higher atomic ratio in NCNT-NH$_3$ compared to previous reports (Table S1), due to using both the organic precursor and ammonia treatment. As for CNT-NH$_3$, the pyridinic N was at very low content of 0.26 at. % (Fig. 3c & d). And as expected, no N atoms of any type were found in CNT-Ar.

3.2. Electrochemical characterizations

The electrochemical CO$_2$ reduction was examined by the linear sweep voltammetry (LSV) in CO$_2$ (Fig. 4a) and Ar (Fig. S5a) saturated 0.5 M NaHCO$_3$ aqueous solution. Current densities of NCNT-NH$_3$ and NCNT-Ar increased sharply at -0.48 V vs RHE and a reduction wave appeared at peak potential of -0.70 V vs RHE under CO$_2$. However, no reduction wave was found under Ar. The peak current at -0.70 V increased linearly with increasing concentrations of NaHCO$_3$ electrolyte (Fig. S6a, b). A plot of log(J) vs log([HCO$_3^-$]) shows a slope of 0.116, suggesting that the reduction wave was independent on HCO$_3^-$ and was due to surface adsorbed species [48]. Also, for CNT-NH$_3$, the reduction peak became smaller, and for CNT-Ar, no reduction peak was found under CO$_2$. Based on the above results, the reduction peak can be assigned as reduction of surface adsorbed CO$_2$. Those results indicate that N doping is beneficial for CO$_2$ reduction reaction.

Controlled potential electrolysis (CPE) was performed to evaluate the product of CO$_2$ reduction. The applied potentials were varied from -0.4 to -1.2 V vs RHE in CO$_2$ saturated 0.5 M NaHCO$_3$ solution. CO and H$_2$ were the only gaseous products and no solution product was detected. NCNT-NH$_3$ showed the highest activity for CO$_2$ reduction reaction (Fig. 4b, c). The onset of electrocatalysis occurred at -0.4 V with CO FE of 62.1%, corresponding to a low overpotential of 0.3 V. The CO current density increased with the applied potential, reaching 22.3 mA cm^{-2} at -1.0 V, and the FE of CO was above 94.5% within the range of -0.6 to -0.9 V. The maximum CO FE reached 96.2% with a decent CO current density of 9.7 mA cm^{-2} at -0.7 V. The CO FE of NCNT-Ar was slightly smaller compared to NCNT-NH$_3$ between -0.6 to -0.9 V (Fig. 4c). With more negative applied potential, the rate of hydrogen evolution reaction increased, resulting in decrease of CO FE. By contrast, the CO FE became much smaller in CNT-Ar and CNT-NH$_3$. The maximum CO FE was 58.8% for CNT-NH$_3$ at -0.7 V. CNT-Ar mainly produced H$_2$ and the maximum FE for CO was only 5.1% at -0.8 V. Control experiments were performed using NCNT-NH$_3$ in Ar saturated 0.5 M NaHCO$_3$ and 0.5 M Na$_2$SO$_4$ aqueous solutions. The FE of H$_2$ exceeds 95% (Fig. S7), indicating that CO arises from CO$_2$, not from the functional groups on the surface of NCNTs.

Electrochemical impedance spectroscopy (EIS) was performed at -0.6 V and the EIS plots were fit with an equivalent electronic circuit (Fig. 5). R_s, R_{ct}, CPE and Z_w denote electrolyte solution resistance, charge-transfer impedance, constant phase element and Warburg impedance, respectively. The R_{ct} of NCNT-NH$_3$ and NCNT-Ar were fit as 54 and 62 Ω, respectively, much lower than the value of 174 Ω for CNT-NH$_3$ and 197 Ω for CNT-Ar. The lower R_{ct} indicates that the electron transfer in NCNT-NH$_3$ is more rapid than others.
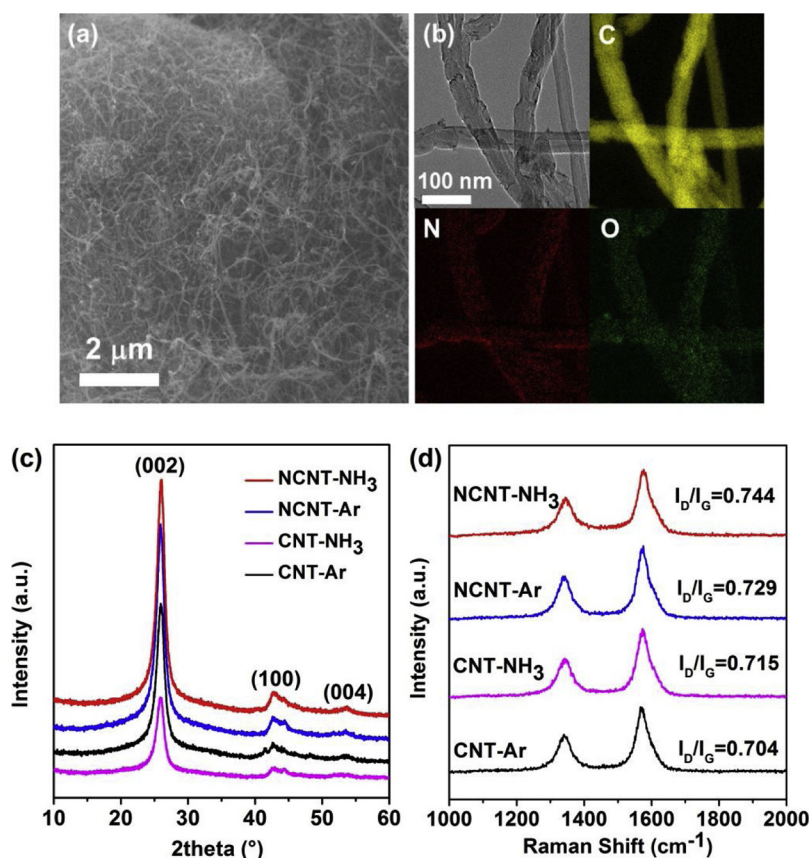
Fig. 2. Material characterizations. (a) SEM image of NCNT-NH$_3$. (b) TEM image of NCNT-NH$_3$ and EELS element mapping of C, N and O. (c) XRD patterns for NCNT-NH$_3$, NCNT-Ar, CNT-NH$_3$ and CNT-Ar. (d) Raman spectra of NCNT-NH$_3$, NCNT-Ar, CNT-NH$_3$ and CNT-Ar.
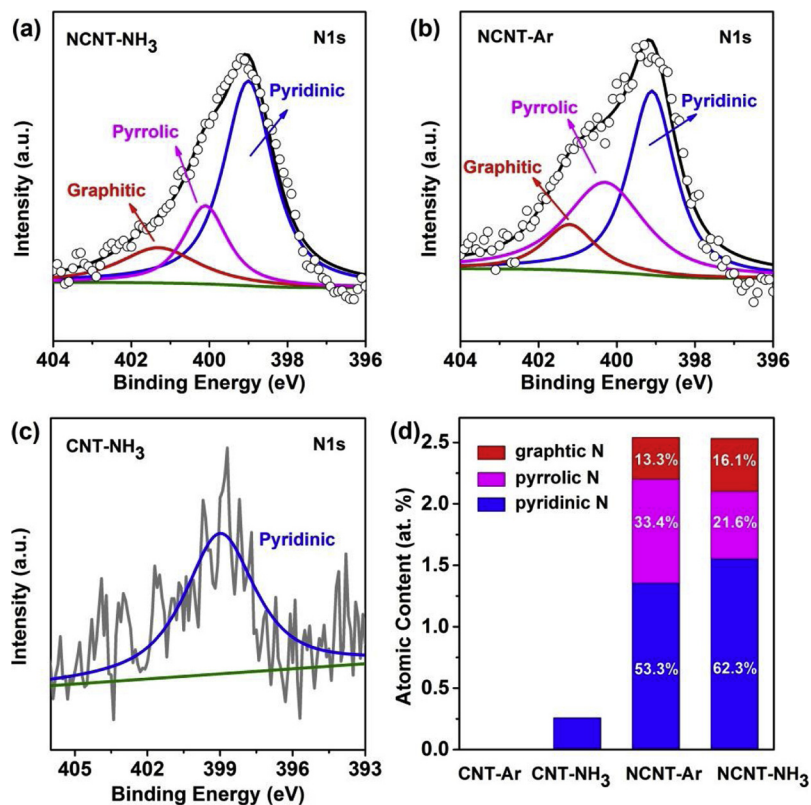

Fig. 3. XPS characterization. (a)–(c) XPS of N 1s spectra for NCNT-NH$_3$, NCNT-Ar and CNT-NH$_3$, respectively, and (d) nitrogen atomic content.
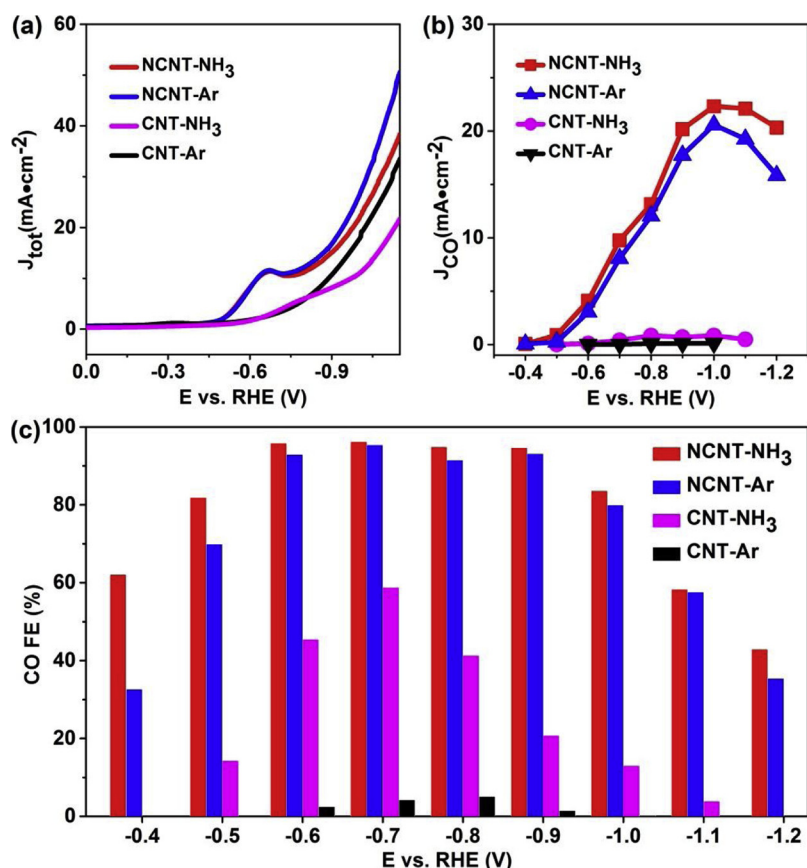
Fig. 4. Electrocatalysis. (a) LSV curves for catalysts in CO_2 saturated 0.5 M $NaHCO_3$ aqueous solution at 50 mV s^{-1}. (b) Partial current density of CO vs applied potential for catalysts. (c) CO FEs at various applied potentials.
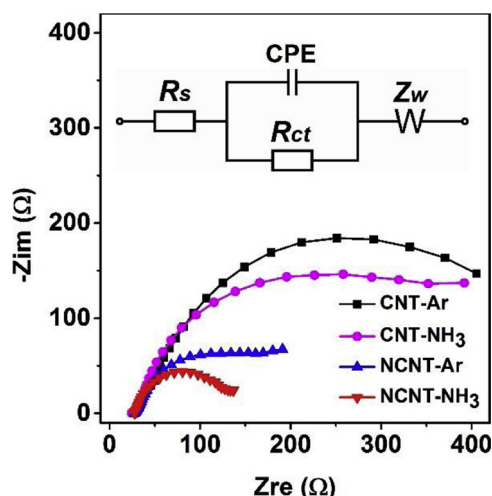

Fig. 5. The Nyquist plots at -0.6 V and equivalent circuit for the catalysts.

3.3. Probing active sites

NCNT-NH$_3$ samples were synthesized at different pyrolysis temperatures. The contents and states of nitrogen in prepared catalysts were shown in Fig. 6. XPS showed that N content increase from at 0.98% to 2.51% with increasing pyrolysis temperature from 300 to 700 °C. NCNT-NH$_3$-700 ranks the highest in the absolute pyridinic N content at 1.56%, followed by 1.20% in NCNT-NH$_3$-500 and 0.78% in NCNT-NH$_3$-300. Interestingly, high pyridinic N percentage of 79.6% can be obtained at low pyrolysis temperature of 300 °C. Low pyrolysis temperature can increase the pyridinic N percentage; however, the

absolute pyridinic N content could be improved at higher temperature. CPE results in Fig. S8 showed that all catalysts were highly selective for CO. The maximum CO FE of 98.6% was achieved at NCNT-NH$_3$-300, which may be contributed by its high pyridinic N percentage. From the results of CPE, high pyridinic N percentage is helpful to increase the FE of CO. In addition, the CO current density increased linearly with content of the pyridinic N at the same applied potential (Fig. 7a), suggesting that the pyridinic N is the main active site for CO$_2$RR.

CO$_2$ temperature-programmed desorption (TPD) results (Fig. S9) showed a broad CO$_2$ desorption peak at 110 °C on NCNT-NH$_3$, assigned to weak chemical adsorption on the catalyst surface. However, only a small peak was found on CNT-NH$_3$ and CNT-Ar, and the desorption temperature was lower. The high desorption temperature indicates relatively strong adsorption between CO$_2$ and catalyst, which can benefit CO$_2$RR [36]. Those data indicate that the adsorption behavior of CO$_2$ was mostly contributed by N sites on NCNT surface.

The electrochemical surface area (ECSA) in NCNT catalysts increased upon N doping. From data in Fig. S10, the ECSA of NCNT-NH$_3$ is nearly the same as NCNT-Ar, but two and four times higher than CNT-NH$_3$ and CNT-Ar, respectively. Higher ECSA suggests more catalytically active sites and could lead to the enhanced activity of NCNT catalysts.

NCNT-NH$_3$ showed high catalytic stability for CO$_2$ reduction. In CPE for 40 h at -0.8 V (Fig. 7b), the CO FE maintained at 95%. XPS was used to investigate the configuration of nitrogen after long-term electrolysis (Fig. S11). In Fig. 7c, after 5 h CPE for CO$_2$RR, the relative concentration of pyrrolic N at 400.1 eV exhibited an obviously increase from 20.9% to 59.5%, and pyridinic N decreased from 62.3% to 40.5%. According to previous reports [28,29,49,50], this result suggests a weak interaction between pyridinic N and CO$_2$, which shares a similar binding energy with pyrrolic N. In the long-term CPE, the relative
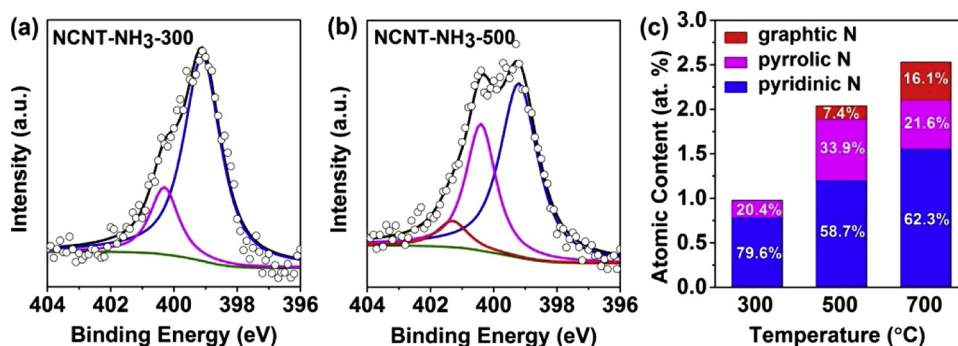
Fig. 6. N1 s spectrum of (a) NCNT-NH$_3$-300 and (b) NCNT-NH$_3$-500, respectively. (c) Nitrogen atomic content vs the temperature of pyrolysis.
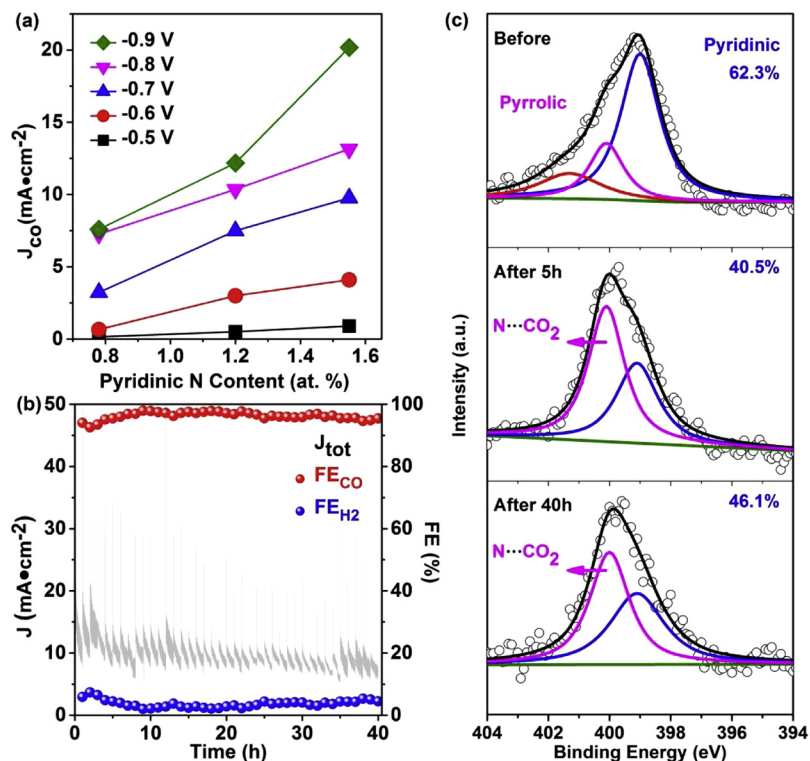

Fig. 7. (a) CO current density at different applied potential vs the content of pyridinic N (at. %). (b) The stability test of NCNT-NH$_3$ at −0.8 V vs RHE in CO$_2$ saturated 0.5 M NaHCO$_3$. (c) The XPS of N1 s for NCNT-NH$_3$ before and after electrolysis.
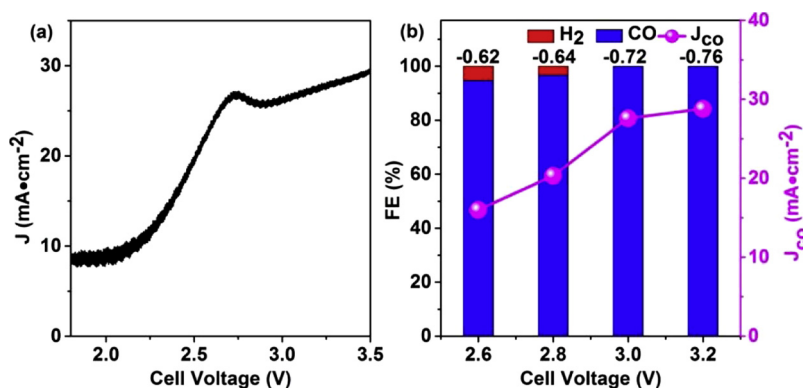

Fig. 8. Gas phase electrolysis in a flow cell. (a) LSV curve, 5 mV s^{-1}. (b) FE of CO (blue) and H$_2$ (red) vs cell voltage (left axis) and partial current density of CO vs cell voltage (right axis), values above the column are cathode potentials vs normal hydrogen electrode (NHE) (For interpretation of the references to colour in this figure legend, the reader is referred to the web version of this article).

concentration of pyridinic N remained a relatively stable value, from 40.5% to 46.1%. Nanoporous structure kept intact in the SEM images of NCNT-NH$_3$ after 40 h electrolysis (Fig. S12). Compared with previous reports in Table S1, NCNT-NH$_3$ exhibited higher activity for CO$_2$ reduction, including high selectivity, current density and long-term stability.

3.4. Gas phase CO$_2$ electrolysis

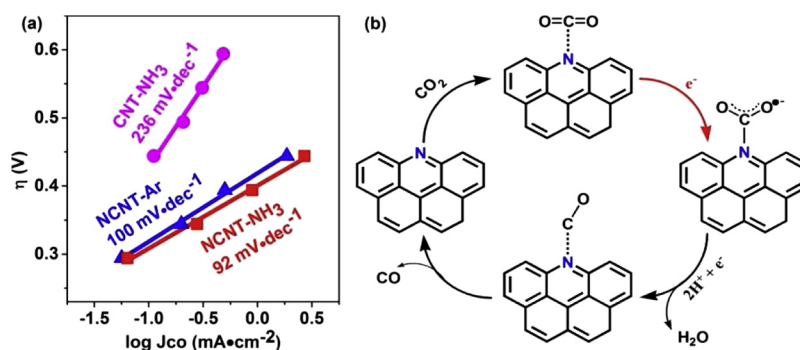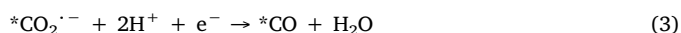Gas phase CO$_2$ electrolyses were performed in a flow cell with a

Fig. 9. (a) Tafel plots for CO formation. (b) Proposed mechanism for the CO_2 reduction reaction on NCNTs.

membrane-electrode assembly (MEA), and the NCNT-NH$_3$ was loaded at the cathode side (Fig. S13). LSV curve in Fig. 8a showed significant current density increasing from the cell voltage of 2 V, and the CO_2 reduction peak can be observed at 2.7 V. In the constant voltage electrolysis, the FE and current density of CO were shown in Figs. 8b & S14a, and only CO can be detected at cell voltage of 3.0 and 3.2 V. This result indicates that hydrogen evolution was almost completely suppressed. The current density of CO increased from 16.8 to 28.8 mA cm^{-2} as cell voltage from 2.6 to 3.2 V (cathode potentials measured to be -0.62 to -0.76 V vs NHE). Moreover, the CO FE kept nearly 100% and the CO current density was stable at 26 mA cm^{-2} in 17 h electrolysis (Fig. S14b). The amount of CO product reached 0.0414 mol. The CO rates and CO_2 conversion values for the gas-phase electrolysis were listed in Table S2. In addition, the catalytic stability was further improved in gas phase CO_2 electrolysis. These results suggest that gas phase CO_2 electrolysis is a viable approach to maximize the CO_2 reduction efficiency, selectivity as well as the catalyst stability.

3.5. Mechanistic study

Tafel analysis was performed to understand the kinetics of CO_2 reduction (Fig. 9a). Tafel slopes were 92 and 100 mV dec^{-1} for NCNT-NH$_3$ and NCNT-Ar, which are relatively small compared to literature reports. Both are less than 118 mV dec^{-1}, indicating faster kinetics for CO formation. According to previous works, the two-electron reduction of CO_2 to CO on NCNTs may follow the following steps [17,48]

$$CO_2 + * \rightarrow *CO_2 \tag{1}$$

$$*CO_2 + e^- \rightarrow *CO_2^{\cdot -} \tag{2}$$

$$*CO_2^{\cdot -} + 2H^+ + e^- \rightarrow *CO + H_2O \tag{3}$$

$$*CO \rightarrow CO + * \tag{4}$$

where the asterisk denotes an active site. As proposed in Fig. 9b, first, CO_2 is adsorbed on the active site, and then accepts one electron to form a surface bound $CO_2^{\cdot -}$. In subsequent steps, the CO_2^- intermediate takes two protons and another electron to form *CO and H$_2$O [17]. Finally, CO is released from active site. However, with strong CO_2 adsorption, electron transfer (eq 2) becomes the rate-determining step (RDS) and the Tafel slopes are less than 118 mV dec^{-1}. The small Tafel slope suggests the benefits of high pyridinic N concentration. According to DFT calculations [30,36,41], the CO binding on NCNT surface is very weak and CO can be de-adsorbed quickly, and it is difficult for *CO to take a proton to complete further reduction process.

The increased catalyst efficiency is attributed to high pyridinic N content in NCNT-NH$_3$. It is consistent with previous reports by Ajayan et al. [41], the energy barrier for pyridinic N in CO_2 reduction is lower than pyrrolic N. From XPS analyses, three types of N exist in carbon nanotubes. The pyridinic N and pyrrolic N are located in a π conjugated system [38]. The pyridinic N in a six-membered ring contributes one p electron to the π system, whereas the pyrrolic N in a five-membered

ring contributes two p electrons [38,51,52]. The graphitic N corresponds to the N species which substitutes for C atoms on the graphite layers [31]. Pyridinic N is a more basic site and easily adsorbs the CO_2 molecule [53], which benefits the subsequent CO_2RR. Using the phenathroline as precursor, the concentration of pyridinic N is significantly increased contributing to more efficient CO_2RR [29,30,33,34,36,39–41].

4. Conclusion

In summary, NCNTs with high atomic abundances of pyridinic N for CO_2RR were synthesized. NCNT-NH$_3$ exhibited outstanding CO_2 reduction performance, and the maximum Faradaic efficiency and current density for CO production reached 96.5% and 22 mA cm^{-2}, respectively. The remarkable performance is due to high concentration of pyridinic N defects. Furthermore, Tafel relation indicates fast kinetics for CO formation at NCNTs. Gas phase electrolysis increases CO_2-catalyst interactions and further improves selectivity and stability. It provides a more efficient process to convert and utilize CO_2 and could be applicable to more types of carbon and metal catalysts.

Appendix A. Supplementary data

Supplementary material related to this article can be found, in the online version, at doi:https://doi.org/10.1016/j.apcatb.2019.03.041.

References

[1] W.R. Peltier, A.M. Tushingham, Global sea level rise and the greenhouse effect: might they be connected? Science 244 (1989) 806–810.
[2] A.M. Appel, J.E. Bercaw, A.B. Bocarsly, H. Dobbek, D.L. DuBois, M. Dupuis, J.G. Ferry, E. Fujita, R. Hille, P.J.A. Kenis, C.A. Kerfeld, R.H. Morris, C.H.F. Peden, A.R. Portis, S.W. Ragsdale, T.B. Rauchfuss, J.N.H. Reek, L.C. Seefeldt, R.K. Thauer, G.L. Waldrop, Frontiers, opportunities, and challenges in biochemical and chemical catalysis of CO_2 fixation, Chem. Rev. 113 (2013) 6621–6658.
[3] E.V. Kondratenko, G. Mul, J. Baltrusaitis, G.O. Larrazabal, J. Perez-Ramirez, Status and perspectives of CO_2 conversion into fuels and chemicals by catalytic, photocatalytic and electrocatalytic processes, Energy Environ. Sci. 6 (2013) 3112–3135.
[4] W. Zhang, Y. Hu, L. Ma, G. Zhu, Y. Wang, X. Xue, R. Chen, S. Yang, Z. Jin, Progress and Perspective of Electrocatalytic CO_2 reduction for renewable carbonaceous fuels and chemicals, Adv. Sci. 5 (2018) 1700275.
[5] H. Zhang, J. Li, Q. Tan, L. Lu, Z. Wang, G. Wu, Metal–organic frameworks and their derived materials as electrocatalysts and photocatalysts for CO_2 reduction: progress, challenges, and perspectives, Chem. - Eur. J. 24 (2018) 18137–18157.
[6] J. Peng, X. Chen, W.-J. Ong, X. Zhao, N. Li, Surface and heterointerface engineering of 2D MXenes and their nanocomposites: insights into electro- and photocatalysis, Chem 5 (2019) 18–50.
[7] Y. Wang, P. Han, X. Lv, L. Zhang, G. Zheng, Defect and interface engineering for aqueous electrocatalytic CO2 reduction, Joule 2 (2018) 2551–2582.
[8] T. Zheng, K. Jiang, H. Wang, Recent advances in electrochemical CO_2-to-CO

conversion on heterogeneous catalysts, Adv. Mater. 30 (2018) 1802066.

[9] J. Wu, T. Sharifi, Y. Gao, T. Zhang, P.M. Ajayan, Emerging carbon-based heterogeneous catalysts for electrochemical reduction of carbon dioxide into value-added chemicals, Adv. Mater. (2018) 1804257, , https://doi.org/10.1002/adma.201804257.

[10] J. Qiao, Y. Liu, F. Hong, J. Zhang, A review of catalysts for the electroreduction of carbon dioxide to produce low-carbon fuels, Chem. Soc. Rev. 43 (2014) 631–675.

[11] D.D. Zhu, J.L. Liu, S.Z. Qiao, Recent advances in inorganic heterogeneous electrocatalysts for reduction of carbon dioxide, Adv. Mater. 28 (2016) 3423–3452.

[12] L. Zhang, Z.-J. Zhao, J. Gong, Nanostructured materials for heterogeneous electrocatalytic CO_2 reduction and their related reaction mechanisms, Angew. Chem. Int. Ed. 56 (2017) 11326–11353.

[13] A. Vasileff, Y. Zheng, S.Z. Qiao, Carbon solving carbon's problems: recent progress of nanostructured carbon-based catalysts for the electrochemical reduction of CO_2, Adv. Energy Mater. 7 (2017) 1700759–1700779.

[14] W. Zhu, Y.J. Zhang, H. Zhang, H. Lv, Q. Li, R. Michalsky, A.A. Peterson, S. Sun, Active and selective conversion of CO_2 to CO on ultrathin Au nanowires, J. Am. Chem. Soc. 136 (2014) 16132–16135.

[15] C. Kim, H.S. Jeon, T. Eom, M.S. Jee, H. Kim, C.M. Friend, B.K. Min, Y.J. Hwang, Achieving selective and efficient electrocatalytic activity for CO_2 reduction using immobilized silver nanoparticles, J. Am. Chem. Soc. 137 (2015) 13844–13850.

[16] K. Sun, T. Cheng, L. Wu, Y. Hu, J. Zhou, A. Maclennan, Z. Jiang, Y. Gao, W.A. Goddard, Z. Wang, Ultrahigh mass activity for carbon dioxide reduction enabled by gold–iron core–shell nanoparticles, J. Am. Chem. Soc. 139 (2017) 15608–15611.

[17] Q. Lu, J. Rosen, Y. Zhou, G.S. Hutchings, Y.C. Kimmel, J.G. Chen, F. Jiao, A selective and efficient electrocatalyst for carbon dioxide reduction, Nat. Commun. 5 (2014) 3242.

[18] Y.S. Ham, S. Choe, M.J. Kim, T. Lim, S.-K. Kim, J.J. Kim, Electrodeposited Ag catalysts for the electrochemical reduction of CO_2 to CO, Appl. Catal. B 208 (2017) 35–43.

[19] Y. Chen, M.W. Kanan, Tin oxide dependence of the CO_2 reduction efficiency on tin electrodes and enhanced activity for Tin/Tin oxide thin-film catalysts, J. Am. Chem. Soc. 134 (2012) 1986–1989.

[20] S. Zhang, P. Kang, T.J. Meyer, Nanostructured tin catalysts for selective electrochemical reduction of carbon dioxide to formate, J. Am. Chem. Soc. 136 (2014) 1734–1737.

[21] F. Lei, X. Zheng, X. Meijia, L. Yingying, L. Zhongjian, 1D SnO_2 with wire-in-tube architectures for highly selective electrochemical reduction of CO_2 to C_1 products, Adv. Funct. Mater. 28 (2018) 1706289.

[22] C.W. Li, M.W. Kanan, CO_2 Reduction at low overpotential on Cu electrodes resulting from the reduction of thick Cu_2O films, J. Am. Chem. Soc. 134 (2012) 7231–7234.

[23] Y.X. Duan, F.L. Meng, K.H. Liu, S.S. Yi, S.J. Li, J.M. Yan, Q. Jiang, Amorphizing Of Cu nanoparticles toward highly efficient and robust electrocatalyst for Co_2 reduction to liquid fuels with high faradaic efficiencies, Adv. Mater. 30 (2018) 1706194.

[24] G. Shan, J. Xingchen, S. Zhongti, Z. Wenhua, S. Yongfu, W. Chengming, H. Qitao, Z. Xiaolong, Y. Fan, Y. Shuyang, L. Liang, W. Ju, X. Yi, Ultrathin Co_3O_4 layers realizing optimized CO_2 electroreduction to formate, Angew. Chem. Int. Ed 55 (2016) 698–702.

[25] S. Gao, Y. Lin, X. Jiao, Y. Sun, Q. Luo, W. Zhang, D. Li, J. Yang, Y. Xie, Partially oxidized atomic cobalt layers for carbon dioxide electroreduction to liquid fuel, Nature 529 (2016) 68–71.

[26] Y. Pan, R. Lin, Y. Chen, S. Liu, W. Zhu, X. Cao, W. Chen, K. Wu, W.-C. Cheong, Y. Wang, L. Zheng, J. Luo, Y. Lin, Y. Liu, C. Liu, J. Li, Q. Lu, X. Chen, D. Wang, Q. Peng, C. Chen, Y. Li, Design of single-atom Co–N_5 Catalytic Site: a robust electrocatalyst for CO_2 reduction with nearly 100% CO selectivity and remarkable stability, J. Am. Chem. Soc. 140 (2018) 4218–4221.

[27] Z. Geng, Y. Cao, W. Chen, X. Kong, Y. Liu, T. Yao, Y. Lin, Regulating the coordination environment of Co single atoms for achieving efficient electrocatalytic activity in CO_2 reduction, Appl. Catal. B 240 (2019) 234–240.

[28] B. Kumar, M. Asadi, D. Pisasale, S. Sinha-Ray, B.A. Rosen, R. Haasch, J. Abiade, A.L. Yarin, A. Salehi-Khojin, Renewable and metal-free carbon nanofibre catalysts for carbon dioxide reduction, Nat. Commun. 4 (2013) 2819.

[29] J. Wu, S. Ma, J. Sun, J.I. Gold, C. Tiwary, B. Kim, L. Zhu, N. Chopra, I.N. Odeh, R. Vajtai, A.Z. Yu, R. Luo, J. Lou, G. Ding, P.J.A. Kenis, P.M. Ajayan, A metal-free electrocatalyst for carbon dioxide reduction to multi-carbon hydrocarbons and oxygenates, Nat. Commun. 7 (2016) 13869.

[30] Y. Song, W. Chen, C. Zhao, S. Li, W. Wei, Y. Sun, Metal-free nitrogen-doped mesoporous carbon for electroreduction of CO_2 to ethanol, Angew. Chem. Int. Ed. 129 (2017) 10980–10984.

[31] X. Duan, J. Xu, Z. Wei, J. Ma, S. Guo, S. Wang, H. Liu, S. Dou, Metal-free carbon materials for CO_2 electrochemical reduction, Adv. Mater. 29 (2017) 1701784–1701803.

[32] H. Wang, Y. Chen, X. Hou, C. Ma, T. Tan, Nitrogen-doped graphenes as efficient electrocatalysts for the selective reduction of carbon dioxide to formate in aqueous solution, Green Chem. 18 (2016) 3250–3256.

[33] J. Wu, M. Liu, P.P. Sharma, R.M. Yadav, L. Ma, Y. Yang, X. Zou, X.-D. Zhou, R. Vajtai, B.I. Yakobson, J. Lou, P.M. Ajayan, Incorporation of nitrogen defects for efficient reduction of CO_2 via two-electron pathway on three-dimensional graphene foam, Nano Lett. 16 (2016) 466–470.

[34] X. Sun, X. Kang, Q. Zhu, J. Ma, G. Yang, Z. Liu, B. Han, Very highly efficient reduction of CO_2 to CH_4 using metal-free N-doped carbon electrodes, Chem. Sci. 7 (2016) 2883–2887.

[35] H. Wang, J. Jia, P. Song, Q. Wang, D. Li, S. Min, C. Qian, L. Wang, Y.F. Li, C. Ma, T. Wu, J. Yuan, M. Antonietti, G.A. Ozin, Efficient electrocatalytic reduction of CO_2 by nitrogen-doped nanoporous carbon/carbon nanotube membranes: a step towards the electrochemical CO_2 refinery, Angew. Chem. Int. Ed. 56 (2017) 7847–7852.

[36] S. Liu, H. Yang, X. Huang, L. Liu, W. Cai, J. Gao, X. Li, T. Zhang, Y. Huang, B. Liu, Identifying active sites of nitrogen-doped carbon materials for the CO_2 reduction reaction, Adv. Funct. Mater. 28 (2018) 1800499.

[37] L. Zhang, J. Xiao, H. Wang, M. Shao, Carbon-based electrocatalysts for hydrogen and oxygen evolution reactions, ACS Catal. 7 (2017) 7855–7865.

[38] X. Wang, Y. Liu, D. Zhu, L. Zhang, H. Ma, N. Yao, B. Zhang, Controllable growth, structure, and low field emission of well-aligned CNx nanotubes, J. Phys. Chem. B 106 (2002) 2186–2190.

[39] S. Zhang, P. Kang, S. Ubnoske, M.K. Brennaman, N. Song, R.L. House, J.T. Glass, T.J. Meyer, Polyethylenimine-enhanced electrocatalytic reduction of CO_2 to formate at nitrogen-doped carbon nanomaterials, J. Am. Chem. Soc. 136 (2014) 7845–7848.

[40] J. Wu, R.M. Yadav, M. Liu, P.P. Sharma, C.S. Tiwary, L. Ma, X. Zou, X.-D. Zhou, B.I. Yakobson, J. Lou, P.M. Ajayan, Achieving highly efficient, selective, and stable CO_2 reduction on nitrogen-doped carbon nanotubes, ACS Nano 9 (2015) 5364–5371.

[41] P.P. Sharma, J.J. Wu, R.M. Yadav, M.J. Liu, C.J. Wright, C.S. Tiwary, B.I. Yakobson, J. Lou, P.M. Ajayan, X.D. Zhou, Nitrogen-doped carbon nanotube arrays for high-efficiency electrochemical reduction of CO_2: on the understanding of defects, defect, density, and selectivity, Angew. Chem. Int. Ed. 54 (2015) 13701–13705.

[42] J.Y. Xu, Y.H. Kan, R. Huang, B.S. Zhang, B.L. Wang, K.H. Wu, Y.M. Lin, X.Y. Sun, Q.F. Li, G. Centi, D.S. Su, Revealing the origin of activity in nitrogen-doped nanocarbons towards electrocatalytic reduction of carbon dioxide, Chemsuschem 9 (2016) 1085–1089.

[43] D.A. Salvatore, D.M. Weekes, J. He, K.E. Dettelbach, Y.C. Li, T.E. Mallouk, C.P. Berlinguette, Electrolysis of gaseous CO_2 to CO in a flow cell with a bipolar membrane, ACS Energy Lett. 3 (2018) 149–154.

[44] P. Hou, X. Wang, Z. Wang, P. Kang, Gas phase electrolysis of carbon dioxide to carbon monoxide using nickel nitride as the carbon enrichment catalyst, ACS Appl. Mater. Interfaces 10 (2018) 38024–38031.

[45] N. Gutiérrez-Guerra, L. Moreno-López, J.C. Serrano-Ruiz, J.L. Valverde, A. de Lucas-Consuegra, Gas phase electrocatalytic conversion of CO_2 to syn-fuels on Cu based catalysts-electrodes, Appl. Catal. B 188 (2016) 272–282.

[46] N. Gutiérrez-Guerra, J.A. González, J.C. Serrano-Ruiz, E. López-Fernández, J.L. Valverde, A. de Lucas-Consuegra, Gas-phase electrocatalytic conversion of CO_2 to chemicals on sputtered Cu and Cu–C catalysts electrodes, J. Energy Chem. 31 (2019) 46–53.

[47] D.M. Weekes, D.A. Salvatore, A. Reyes, A. Huang, C.P. Berlinguette, Electrolytic CO_2 reduction in a flow cell, Acc. Chem. Res. 51 (2018) 910–918.

[48] Y. Chen, C.W. Li, M.W. Kanan, Aqueous CO_2 reduction at very low overpotential on oxide-derived Au nanoparticles, J. Am. Chem. Soc. 134 (2012) 19969–19972.

[49] E. Barton Cole, P.S. Lakkaraju, D.M. Rampulla, A.J. Morris, E. Abelev, A.B. Bocarsly, Using a One-electron shuttle for the multielectron reduction of CO_2 to methanol: kinetic, mechanistic, and structural insights, J. Am. Chem. Soc. 132 (2010) 11539–11551.

[50] G. Tuci, J. Filippi, H. Ba, A. Rossin, L. Luconi, C. Pham-Huu, F. Vizza, G. Giambastiani, How to teach an old dog new (electrochemical) tricks: aziridine-functionalized CNTs as efficient electrocatalysts for the selective CO_2 reduction to CO, J. Mater. Chem. A Mater. Energy Sustain. 6 (2018) 16382–16389.

[51] J. Casanovas, J.M. Ricart, J. Rubio, F. Illas, J.M. Jiménez-Mateos, Origin of the large N 1s binding energy in X-ray photoelectron spectra of calcined carbonaceous materials, J. Am. Chem. Soc. 118 (1996) 8071–8076.

[52] D. Wei, Y. Liu, Y. Wang, H. Zhang, L. Huang, G. Yu, Synthesis of N-doped graphene by chemical vapor deposition and its electrical properties, Nano Lett. 9 (2009) 1752–1758.

[53] D. Guo, R. Shibuya, C. Akiba, S. Saji, T. Kondo, J. Nakamura, Active sites of nitrogen-doped carbon materials for oxygen reduction reaction clarified using model catalysts, Science 351 (2016) 361–365.